Received: 24 August 2021 | Revised: 14 October 2021 | Accepted: 19 October 2021

DOI: 10.1002/mrm.29075

TECHNICAL NOTE

Magnetic Resonance in Medicine

The impeded diffusion fraction quantitative imaging assay demonstrated in multi-exponential diffusion phantom and prostate cancer

Dariya I. Malyarenko[1] | **Scott D. Swanson**[1] | **Sean D. McGarry**[2] | **Peter S. LaViolette**[2] | **Thomas L. Chenevert**[1]

[1]Department of Radiology, University of Michigan Medical School, Ann Arbor, Michigan, USA

[2]Department of Radiology and Biomedical Engineering, Medical College of Wisconsin, Milwaukee, Wisconsin, USA

Correspondence
Dariya I. Malyarenko, Department of Radiology, University of Michigan Medical School, 1500 E. Medical Center Dr., Rm UH B2A209, Ann Arbor, MI 48109-5030, USA.
Email: dariya@umich.edu

Funding information
National Institutes of Health, Grant/Award Numbers: U01CA166104, U24CA237683, R01CA249882, R01CA218144, and R01CA190299

Purpose: To demonstrate a method for quantification of impeded diffusion fraction (IDF) using conventional clinical DWI protocols.

Methods: The IDF formalism is introduced to quantify contribution from water coordinated by macromolecules to DWI voxel signal based on fundamentally different diffusion constants in vascular capillary, bulk free, and coordinated water compartments. IDF accuracy was studied as a function of b-value set. The IDF scaling with restricted compartment size and polyvinylpirrolidone (PVP) macromolecule concentration was compared to conventional apparent diffusion coefficient (ADC) and isotropic kurtosis model parameters for a diffusion phantom. An in vivo application was demonstrated for six prostate cancer (PCa) cases with low and high grade lesions annotated from whole mount histopathology.

Results: IDF linearly scaled with known restricted (vesicular) compartment size and PVP concentration in phantoms and increased with histopathologic score in PCa (from median 9% for atrophy up to 60% for Gleason 7). IDF via non-linear fit was independent of b-value subset selected between b = 0.1 and 2 ms/μm^2, including standard-of-care (SOC) PCa protocol. With maximum sensitivity for high grade PCa, the IDF threshold below 51% reduced false positive rate (FPR = 0/6) for low-grade PCa compared to apparent diffusion coefficient (ADC > 0.81 μm^2/ms) of PIRADS PCa scoring (FPR = 3/6).

Conclusion: The proposed method may provide quantitative imaging assays of cancer grading using common SOC DWI protocols.

KEYWORDS
clinical oncology DWI, collective coordinated diffusion, impeded diffusion fraction (IDF), macromolecular density, sub-cellular compartment

1 | INTRODUCTION

Diffusion weighted imaging (DWI) based on endogenous contrast sensitive to tissue microstructure[1] is an appealing imaging modality for non-invasive cancer screening, active surveillance, and longitudinal treatment response monitoring.[2,3] Notwithstanding major advances in acquisition and quantitative (q)DWI models,[4–6] the majority of current clinical MRI protocols continue to use DWI qualitatively as an indicator of impeded diffusion evident from sustained signal at high b-values.[7,8] When quantitation is desired, typically a mono-exponential (ME) diffusion model is used to derive apparent diffusion coefficient (ADC)[9–11] from the fit of DWI signal dependence on b-value. When clinical ADC acquisition protocols are standardized and uniformly implementable across different MRI vendors, reasonably repeatable ADC results may be achieved for multiple organs.[11]

The ADC parameter is moderately correlated (inversely) to Gleason score [GS]) and is the only quantitative DWI metric currently used clinically to aid differentiation of indolent from aggressive prostate cancer (PCa).[8,9] Although PCa remains a high occurrence disease affecting over 248 000 men in 2021,[12] only 10%–15% of PCa patients tend to develop aggressive malignancy requiring radical treatment. For the majority, active surveillance of low-grade disease[13] using noninvasive prostate MRI would improve patient quality-of-life over a prostate biopsy.[14] Prostate Imaging Reporting Data System (PIRADS) PCa scoring schema[8,9] based on multi-parametric MRI (mpMRI), currently uses ADC derived from b ≤ 1000 s/mm^2, and qualitative high-b (>1400 s/mm^2) DWI to indicate diffusion restriction as a component of PCa risk stratification. By including quantitative ADC thresholds, the European Association of Urology expected to reduce unnecessary biopsies by ~30%.[9,15]

However, because of inherently multi-exponential diffusion in the complex tumor micro-environment,[1–3] ADC values depend on technical acquisition features (e.g., b-range and SNR),[4,16] which limits the clinical robustness of quantitative differentiation between indolent and aggressive PCa. Furthermore, because of limited SNR, high-b DWI is currently used only qualitatively,[8] and not included for ADC calculation. All these limitations potentially contribute to a substantial false positive rate at ~70% for low-grade PCa stratification.[9,15] To describe the observed deviation of DWI signal from ME decay, multi-exponential diffusion models introduce additional parameters allowing non-Gaussian (b-range dependent) decay rate[4,17,18] and multiple diffusion compartments.[6,19,20]

Several groups actively seek clinical translation of alternative DWI-derived metrics based on multi-compartment biophysical PCa tumor diffusion models and their correlation to tumor pathology.[17,19,21] To adequately quantify multi-exponential DWI, these multi-parametric methods require specialized wide b-range acquisition and analysis protocols,[17,19,21] with fit algorithms constrained to prevent non-physical parameters ranges (e.g., for perfusion and kurtosis component).[4,5,17] They also commonly rely on organ-dependent assumptions about (population-average) compartment characteristics.[6,19,20] These preclude straightforward extrapolation of the applied diffusion models to multiple organs. Widespread clinical adaptation of the corresponding DWI protocols is further hampered by required prolonged multi-b acquisition and high resolution/SNR not reliably achieved in a clinical setting.[11,22]

The purpose of this work is to introduce a generalized quantitative metric that summarizes non-Gaussian (compartmentalized and impeded) diffusion in the tissue/tumor environment, nominally independent of organ, thereby reducing complexity of the required clinical DWI acquisition protocol. Here, we propose a method that deduces multi-compartment formalism suitable for standard of care (SOC) clinical DWI acquisition protocols to quantify impeded diffusion fraction (IDF) representing the component of water coordinated around macromolecules. The IDF descriptor could have potential value for a wide range of cancer imaging applications (e.g., prostate, breast, and pancreas). In this work, the IDF model with built-in constraints is calibrated using a 2-compartment diffusion kurtosis phantom,[23] and its application is demonstrated for retrospective analysis of the PCa DWI annotated from whole mount histopathology.[16]

2 | METHODS

For phantom and PCa cases, IDF performance was compared to conventional ADC via the mono-exponential diffusion model[1] and non-Gaussian diffusion kurtosis (DK) model[5] for PCa SOC b-value protocols[9]:

$$\log\left(\frac{S_b}{S_0}\right) = K_1 - ADC \bullet b;\quad K_1 = \log(F_{ADC}), \tag{1}$$

$$\log\left(\frac{S_b}{S_0}\right) = -\mathrm{D_a b} + \mathrm{K_a}\left(\mathrm{D_a b}\right)^2/6. \tag{2}$$

Here, F_{ADC} represents the fraction of slow (perfusion-suppressed) diffusion signal, S_b, whereas D_a and K_a are apparent diffusion and kurtosis parameters of the DK model.

2.1 | IDF model

The IDF model parameters, distance scales and built-in constraints[24] are illustrated in Figure 1 and detailed in

Supporting Information. Briefly, IDF formalism hypothesizes that DWI signal originates from compartments having distinct mobility regimes (Figure 1, top) for free (D_f), vascular (D_p), and coordinated (D_i) water. The objective of the IDF approach is to quantify impeded diffusion fraction of water coordinated by membranes and macromolecules (e.g., Figure 1, left), with diffusion an order of magnitude slower than free water, $D_i << D_f$.[25–27] This is achieved by isolating fractional contributions of water from uncoordinated (free) intra/extra-cellular, F_{fc}, bulk free, F_f, and the vascular/capillary space, F_p, (Figure 1 and Supporting Information). To quantify these fractions, the model factors out molecular concentration dependence of nanoscale Arrhenius diffusion in (sub)cellular space, $D_c \approx F_{fc}D_f + IDF \times D_i \rightarrow F_{fc}D_f$ (Figure 1, left), exploits known free water diffusivity, D_f = 3 μm^2/ms (at body temperature),[25] and assumes negligible perfusion signal (→0) above moderately low b-values (>.1 ms/μm^2) for fast vascular pseudo-diffusion (Figure 1, middle), $D_p >> D_f$.[28]

Over typical clinical PCa SOC b-range of 0.1 < b(ms/μm^2) < 2,[9] this allows the following approximation for the DWI signal S_b, measured as a function of b-value:

$$\frac{S_b}{S_0} = \sum_j^{f,p,c} F_j E_j \approx F_f E_f + \left(1 - F_p - F_f\right) E_c; \quad E_{c,f} = \exp\left(-bD_{c,f}\right); D_c \approx F_{fc} D_f \tag{3}$$

$$IDF = 1 - F_p - F_f - F_{fc}. \tag{4}$$

Here, F_j denotes the compartmental fractions (Figure 1, table) from capillary pseudo-diffusion ($j = p$), bulk free ($j = f$), and intra/extra cellular ($j = c$) water, contributing to DWI voxel signal exponentially decaying with increasing b-value and diffusion constant, $E_j = \exp(-bD_j)$. Subcellular uncoordinated fraction, F_{fc}, describes molecular crowding effect on diffusion value, D_c, in subcellular compartment (Supporting Information), and D_f is a

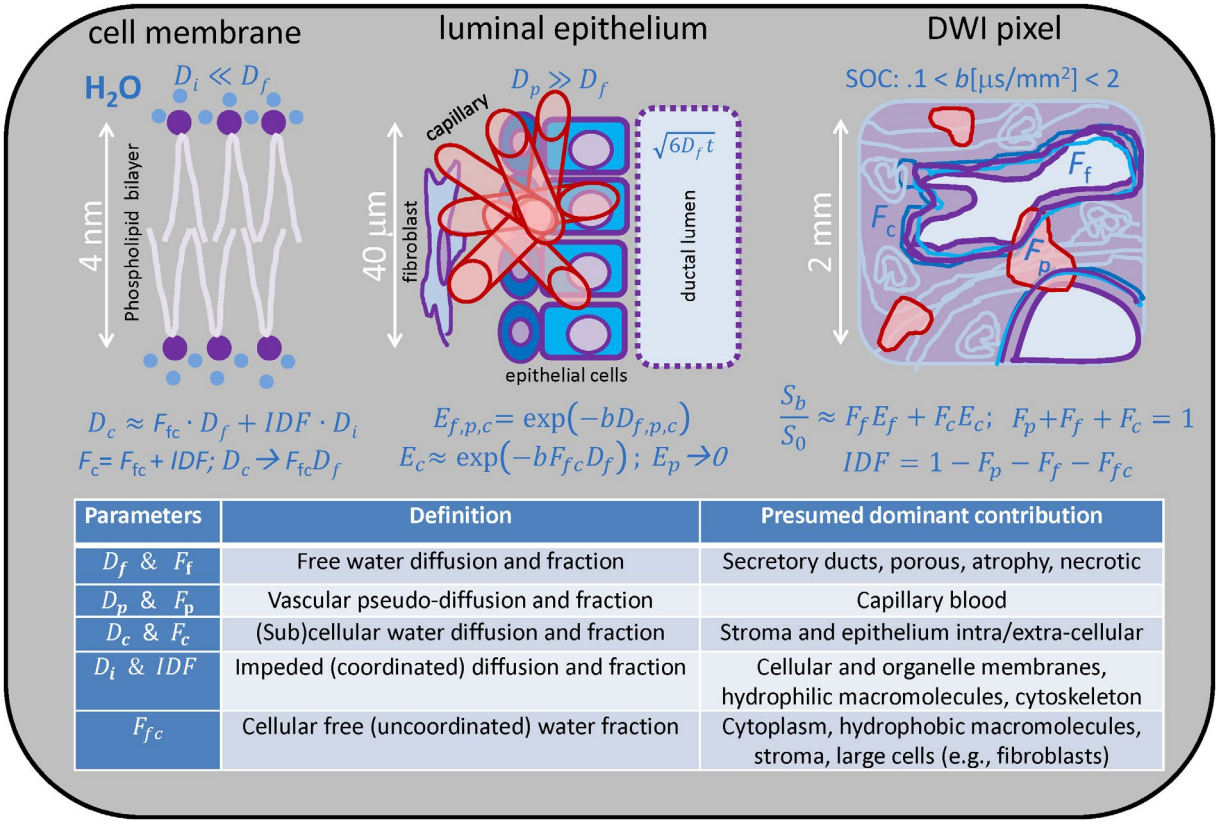

Parameters	Definition	Presumed dominant contribution
D_f & F_f	Free water diffusion and fraction	Secretory ducts, porous, atrophy, necrotic
D_p & F_p	Vascular pseudo-diffusion and fraction	Capillary blood
D_c & F_c	(Sub)cellular water diffusion and fraction	Stroma and epithelium intra/extra-cellular
D_i & IDF	Impeded (coordinated) diffusion and fraction	Cellular and organelle membranes, hydrophilic macromolecules, cytoskeleton
F_{fc}	Cellular free (uncoordinated) water fraction	Cytoplasm, hydrophobic macromolecules, stroma, large cells (e.g., fibroblasts)

FIGURE 1 Water diffusion scales from nanometer to millimeter: IDF DWI model with built-in constraints (top) for relative diffusion values and standard of care (SOC) acquisition protocol b-range. Left: nanoscale water coordination, IDF (D_i < 0.03 μm^2/ms), near cell membrane (or macromolecules) effecting cellular diffusion, D_c, in combination with uncoordinated solvent water fraction, F_{fc}. Middle: mixed diffusion in cells (e.g., stromal fibroblast, purple and ductal epithelium, cyan, and blue), pseudo-diffusion in randomly oriented capillary (red outline, D_p > 30 μm^2/ms), and free diffusion in luminal space (light blue, D_f = 3 μm^2/ms). Right: partial volume contributions to DWI signal from cellular, F_c, bulk free, F_f, and perfused, F_p, tissue for typical clinical DWI pixel (2 × 2 mm^2). Increasing water coordination is depicted by changing color shades from light blue to dark purple. Equations summarize IDF formalism and built-in constraints for measured DWI signal, S_b, and table lists model parameter definitions with examples of presumed dominant contribution

constant free water diffusivity.[25] The model fit sensitivity to IDF detection is enhanced for $1 < b(ms/\mu m^2) < 2$, by suppression of free water contribution (Supporting information, Equation S3).

2.2 | Phantom DWI

Physical origin of IDF versus ADC and DK parameters was studied using a previously described quantitative multi-compartment diffusion phantom[23] (Figure S1A). Vials V1 and V2 provided model systems that consisted of bulk free and impeded vesicular water compartments with controlled vesicle size ratio of V1(2.8 μm): V2(1.6 μm)~1.8. V3 and V5 containing polyvinylpyrrolidone (PVP) concentrations of 20% and 40% supplied a single nanoscale (<10 nm)[29] compartment with macromolecule hydration-coordination and a ME diffusion coefficient that scaled with inverse solute concentration ($\frac{F_{fc}(V5)}{F_{fc}(V3)} = D_c(V3) / D_c(V5) = 1.3/0.6\sim2$). The phantom DWI were acquired using b = 0, 0.05, 0.1, 0.2, 0.5, 0.8, 1, 1.5, 2, 2.5, 3 ms/μm^2, TE = 105 ms, TR = 10 s, voxel-size (VS) = $1.7 \times 1.7 \times 5$ mm^3. Additional cetearyl alcohol (CA) cetyltrimethylammonium bromide (CTAB) vesicle samples (V7 derivatives[30]) with molar ratios from 3:1 to 6:1 (0.7 to 1.7 μm sizes), and PVP solutions of 10%, 30%, and 50%, were used for IDF calibration (Figure S2B).

2.3 | PCa DWI

The studied in vivo multi-b DWI data sets for prostate cancer (PCa) were acquired[16] at the Medical College of Wisconsin (MCW) and shared as de-identified DICOM. The recruited subjects underwent radical prostatectomy for PCa and provided informed consent to participate in the prospective imaging study approved by MCW institutional review board (IRB). The PCa DWI were acquired using endo-rectal (E-R) coil for 10 b-values (b = 0, 0.010, 0.025, 0.05, 0.08, 0.1, 0.2, 0.5, 1, and 2 ms/mm^2) with TE = 68 ms (3 subjects) and 99 ms (3 subjects); TR = 4 s; 4 mm thick slices and in plane resolution 1.5 x 1.5 mm^2 (2 subjects) and 2 x 2 (4 subjects). Ability of IDF model to reflect lesion characteristics was studied for six PCa subjects with both Gleason score (GS) 6 and 7 annotated from whole mount histopathology that was registered to T2-weighted images (Figure S1B, [Hurrel et al][16]). The image annotations also included atrophy, but were not labeled for normal tissue. Selected six subjects had lesions that spanned three DWI slices and had linear size > 1cm.

2.4 | Data analysis

All voxel-by-voxel image model fits and statistical analysis were automated using MATLAB R2019b (The Mathworks, Natick, MA). The parametric maps were generated by fitting diffusion models to the DWI voxel signal dependence on b-value Equations (1)-(4). Conventional SOC ADC fit (Equation 1) used b-values $.1 < b < 1$ ms/μm^2, corresponding to PIRADS v2.1,[8] whereas kurtosis fit (Equation 2) was performed for a 3-b PCa SOC subset (Figure S1B). The nonlinear fit for IDF model (Equation 3) was implemented for F_p, F_f, and F_{fc} of the phantom and PCa datasets (Figure S1) to derive IDF (Equation 4). All fit fractions were constrained between 10^{-4} and 1, with additional constraint for in vivo $F_{fc} < 0.9$. Nonlinear 3-parameter fit was based on trust region reflective algorithm using built-in MATLAB *lsqcurvefit* function with 2000 maximum iterations, fit parameter tolerance of 10^{-5}, and function tolerance of 10^{-6} and took under 3.5 min per slice. Linear fits of ADC and DK models were performed for log-signal intensities using MATLAB build in *lscov* function, and vectorized for the whole DWI volume (under 10-s processing time). The same region of interests (ROIs) were applied to all quantitative parametric maps.

For phantom analysis, free water diffusivity, $D_f = 2.15$ μm^2/ms, was measured at room temperature with $b_{max} = 1.5$ ms/μm^2. IDF dependence on b-range was compared for 7 (non-0) b-values $.1 < b < 2.5$ ms/μm^2 versus clinical PCa SOC b-value subsets (b = 0.1, 0.8, 1.5 ms/μm^2) and (b = 0.2, 1, 2 ms/μm^2) for phantom (Figure S1A), and a single SOC subset was used for the PCa IDF analysis (Figure S1B). Diffusion metric measurements for phantom vials were performed by placing 1×1 cm square ROIs on parametric maps. Relative performance of fit DWI metrics was compared for ROI mean diffusion parameters as a function of phantom vesicle sizes and PVP concentration (Figure S2).

For the PCa analysis, free water diffusion was held fixed at $D_f = 3$ μm^2/ms[25] assuming 37°C subject body temperature. The lesion boundaries were defined on b = 0 registered to T_2-weighted images. The ROI was the ROI was manually defined on a middle lesion slice with 1 acquired voxel (2 mm) away from boundary in each dimension to minimize partial volume effects. The acquired DWI voxel resolution limited lesion sizes that could be analyzed reliably to above 6×6 mm in plane and 12 mm through slice. The DWI registration and lesion segmentation challenges were common for all DWI metrics, and their details are beyond the scope of the present analysis. The protocol induced T_2-weighting bias (different TE) for three PCa subjects was corrected by forward analytical simulation in Supporting Information Equation (S4).[20] Briefly, for DWI

acquisitions with TE = 69 ms, fit F_p was increased by 1%, F_f increased by 7%, and IDF decreased by 8%. The median and ranges of all DWI metric for six subjects were compared for GS7, GS6, and atrophy ROIs, corresponding to provided pathology labels.

3 | RESULTS

The proposed IDF model exhibited good fit fidelity (low fit errors) both for multi- and mono-exponential DWI signal decay with b-value observed in phantom and in vivo (Figure S1 and Table S1). The fit fractions for phantom reflected water content in bulk free (e.g., V2) and coordinated compartments (e.g., V3). Among single voxel fit-fractions (Table S1), IDF provided the highest contrast between GS6 and GS7 cancers (11%), as well as, GS7 cancer versus apparent normal transition zone (nTZ, 40%). Fit IDF was nominally independent (difference under ±1%, data not shown) of the selected subset (7 or 3 SOC b > 0).

3.1 | Phantom parametric maps: relation to physical properties

Comparison of parametric maps of different diffusion models (Figure 2) for the DWI phantom elucidates relation among fit contrasts and undelaying physical properties. For ME diffusion medium in V3 and V5, relative ADC and D_a exhibited scaling similar to F_{fc} = 1-IDF (reverse of the PVP concentration) (Figure S2B). Their observed kurtosis, K_a, and bulk free water fraction, F_f, were appropriately close to 0. For two-compartment vesicular materials in V1 and V2, relative F_f scaled similar to D_a and K_a contrasts and reverse of IDF. Fit perfusion fraction was appropriately absent, and F_{fc} + F_f contribution effectively eliminated in the IDF map with finite SNR-induced degeneracy near fit F_f ~1 (middle vial and bulk surrounding water). The IDF map evidently summarized increasing water coordination both for single and two-compartment diffusion materials on a positive linear (fraction) scale (Figure 2 and Figure S2B).

Quantitatively, relative IDF and $1/D_a$ contrasts scaled linearly with vesicle size (volume to surface ratio [V/S], e.g. V2:V1 ~1.8) and PVP concentration (V3:V5 ~2) (Figure S2A), whereas K_a and 1/ADC ratios did not properly reflect micro-restriction within vesicles. Relative D_a contrast (V2:V1 ~1.7) was a better representation of phantom compartment sizes than K_a (V2:V1 ~1.2) (Figure S2A). IDF calibration revealed a linear relationship between IDF and DLS V/S for micro-vesicles between 0.5 and 3 μm (Figure S2B, lower axis), largely independent of tested chemical constituents. IDF was also linearly increasing with the PVP concentration between 10% and 50% (Figure S2B, top axis).

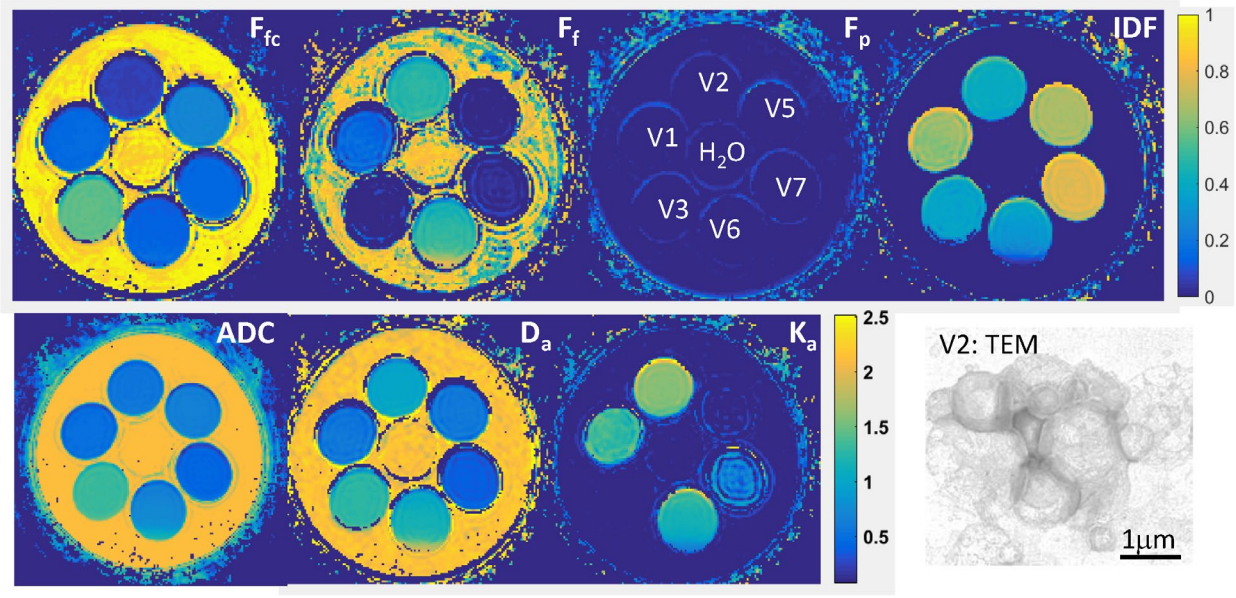

FIGURE 2 Parametric maps for IDF model nonlinear fit fractions of quantitative kurtosis phantom are shown in top row (left-to-right): F_{fc}, F_f, F_p, and IDF. Bottom row shows parametric maps derived from linear fits for PIRADS ADC(b_{max} = 1 ms/μm^2), D_a (μm^2/ms) and K_a, and includes an example transmission electron microscopy (TEM) image of the micro-scale vesicles in vial 2 (V2) sample. Phantom material-vial labels are marked on F_p map. Common scale for all fraction-maps is shown on the right color-bar, whereas metric-specific color-bars accompany ADC, D_a, and K_a parametric maps. Except ADC and D_a (units of μm^2/ms), all map scales are dimensionless

3.2 | PCa IDF versus ADC and DK maps: clinical relevance

Similar to phantom results, prostate IDF (Figure 3) effectively eliminated the free (luminal) water contribution from large (sub-mm) secretory ducts and blood vessels confounding the D_a map in transition zone (nTZ) and prostate base. Compared to D_a, K_a or ADC, IDF also visually enhanced contrast between peripheral zone (PZ) atrophy (ATR, low IDF) and nTZ tissue. For the GS6/GS7 lesion of this subject, IDF evidently captured complementary $K_a \sim 1/D_a$ contrast information, visually most similar to 1/ADC and $1/D_a$, but on a linear (fraction) scale.

Quantitative diffusion metrics for lesions that had pathology annotations (GS7, GS6, and atrophy) are summarized in Table 1. Prostate IDF scaled positively and linearly with the lesion grade, increasing from median 9% (range, 2%–13%) for atrophy to 44% (31%–50%) for GS6 and to 60% (51%–71%) for GS7. Among individual fit fractions, the largest decrease (from 66% down to 21%) with increasing lesion grade was observed for F_f, whereas F_p (changing only from 7% to 5%.) was the least sensitive fit metric. Compared to GS6 and GS7, atrophy also had notably (~60%) higher ADC and D_a, and (~55%) lower K_a. It is worth noting that accuracy of all derived DWI metrics would depend on lesion segmentation, whereby errors confound ROI parameter values by partial volume effects. This is particularly challenging for small targets (Figure S1B) (e.g., GS6), when narrow linear cancer lesions are adjacent to atrophy. Low IDF thresholds could help reliable atrophy segmentation.

Figure 4 compares diagnostic performance for 12 PCa lesions when GS7 true positive rate (TPR) threshold is set at 1 (maximum GS7 sensitivity). The results indicate reduced IDF false positive rate (FPR = 0/6) (Figure 4A) for GS6 versus GS7 lesion differentiation in contrast to standard PIRADS ADC (FPR = 3/6) (Figure 4B). These preliminary findings also suggest that IDF threshold above 51% (Figure 4A, magenta line) could be used for detection of aggressive prostate cancers as reliably as PIRADS ADC $< 0.81\ \mu m^2/ms$ (Figure 4B, magenta line), but with lower FPR. The IDF discriminative power originated almost entirely from fit $F_f > 27\%$ for GS6 (other fit fractions comparable for GS6 vs. GS7, data not shown). With maximum GS7 sensitivity, FPR = 0/6 was also observed for $D_a < 1.05\ \mu m^2/ms$ (Figure 4C), however, the related kurtosis model parameter $K_a > 0.8$ showed high FPR = 5/6 (Figure 4D). Overall, the observed performance of PCa DWI metrics correlated with their ability to reflect the size of vesicle compartment in the phantom (Figure S2A).

4 | DISCUSSION

The proposed IDF model demonstrated several benefits; it effectively suppressed free and pseudo-diffusion water

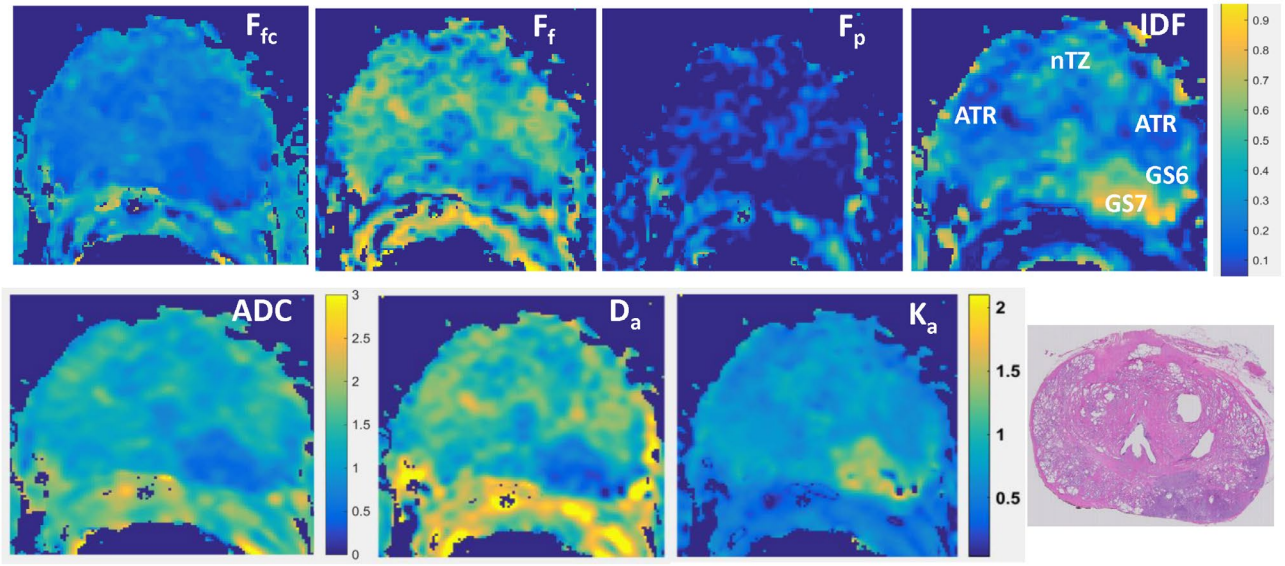

FIGURE 3 Parametric maps for IDF model nonlinear fit fractions of an example PCa subject are shown in top row (left-to-right): F_{fc}, F_f, F_p, and IDF. Bottom row shows parametric maps derived from linear fits for PIRADS ADC(b_{max} = 1 ms/μm^2), D_a (μm^2/ms), and K_a, as well as the corresponding hematoxylin and eosin (H&E) stained example image. Common value-scale for all fraction-maps is shown on the right color-bar, whereas metric-specific color-bars accompany ADC, D_a, and K_a parametric maps. Except ADC and D_a (units of μm^2/ms), all map scales are dimensionless. PCa parametric maps are shown for a single slice image with right-left atrophy (ATR) and mixed GS7 (geographic) adjacent to GS6 (linear) tumor lesions in base right peripheral zone (PZ), corresponding to histopathology labeling from Hurrel et al,[16] and normal transition zone (nTZ, middle)

TABLE 1 Summary of quantitative DWI metric (median [range]) for IDF fit fractions (±1%), PIRADS ADC, D_a, and K_a across six PCa subjects for lesion ROIs of GS7, GS6, and ATR annotated from whole-mount histopathology[16]

Metric/ lesion median [range]	GS7	GS6	ATR
F_p (%)	6.5 [0, 10]	7 [2.5, 13]	5 [0, 6]
F_f (%)	21 [17, 27]	32 [28, 54]	66 [45, 72]
F_{fc} (%)	16 [13, 21]	17 [15, 25]	29 [20, 42]
IDF (%)	60 [51, 71]	44 [31, 50]	9 [2, 13]
ADC (μm^2/ms)	0.68 [0.55, 0.81]	0.8 [0.7, 1.1]	1.75 [1.62, 1.96]
D_a (μm^2/ms)	0.96 [0.66, 1.05]	1.19 [1.14, 1.64]	2.34 [2.06, 2.78]
K_a	1.14 [0.8, 1.35]	1.03 [0.76, 1.12]	0.54 [0.47, 0.56]

Abbreviations: ATR, atrophy; GS, Gleason score.

background (e.g., from capillary and luminal water) and was independent of b-value subset within SOC DWI b-range. Therefore, unlike conventional ADC metric dependent on b-range,[16] nonlinear IDF model fit would be more robust to the typical variations in clinical acquisition protocols. IDF reported on water fraction coordinated by macromolecules and scaled linearly with micro-compartment size and macromolecular concentration in a phantom. The model did not rely on organ-specific compartment assumptions, and may be applied to evaluate tumor grade in multiple malignancies. For the small studied PCa dataset, IDF outperformed PIRADS ADC and apparent kurtosis parameters in its ability to quantify changing sizes of microscale compartments in phantom and showed promise to reduce FPR for low versus high grade PCa stratification. The described diagnostic performance results are preliminary given the major limitation of the small study sample. Among conventional model metrics, inverse of apparent diffusion parameter for the kurtosis model performed most similar to IDF. Notably, in studied PCa lesions, increase in IDF was predominantly caused by reduction in free (e.g., luminal) water fraction, consistent with the independent studies of luminal water fraction by multi-echo T_2 relaxometry experiments.[31,32]

The IDF model has several limitations; it does not specifically inform on location of the macromolecular coordination surface (extra- vs. intra-cellular) and exhibits finite degeneracy because of SNR bias when combined free and uncoordinated water fractions are close to 1. This would tend to be the case for porous (e.g., atrophy or necrotic) tissue. Although performed phantom analysis revealed IDF correlation to sizes of membranous structures and macromolecule concentration, more detailed histologic studies are warranted to establish tissue fraction equivalents of the IDF model parameters. The noise floor bias could also be addressed by including noise model, which would require acquisition of more b-values. Importantly, the derived fit fractions are T_2 and T_1 weighted,[20] hence, would depend on acquisition TE and TR, and would benefit from DWI protocol standardization. This protocol-dependent bias may be accounted for retrospectively by analytical simulation of relaxation dependence as was demonstrated in this work. Additionally, the collective diffusion for coordinated water is expected to depend on distribution of macromolecule sizes[27] that may partially violate model constraints for high b-values (1.5~2 ms/μm^2). The model does not describe diffusion anisotropy and time dependence and cannot be directly compared to the multi-compartment methods that probe these quantities based on specialized acquisition protocols.[19,21]

Acquisition protocol consistency and bias estimates would facilitate establishing more robust diagnostic thresholds for an IDF-based assay. Because the suggested thresholds of PCa IDF > 51% (for GS7) were determined for a small sample of 12 lesions and good SNR provided by E-R coil, they may need to be adjusted in larger study sampling wider ranges of lesion grades with different coils. The absolute thresholds will likely depend on acquisition TR and TE because of compartmental T_1- and T_2-weighting bias.[20] This could be mitigated for by analytical modeling using nominal compartment T_1 and T_2 values[33,34] as demonstrated here. Because both IDF model and acquisition protocols do not include organ-dependent assumptions, the proposed assay strategy can be potentially generalized to multiple organ cancers, although different assay thresholds are expected for different malignancies. Larger studies would be required to establish practical clinical value (sensitivity and specificity) of the developed imaging assays.

IDF contrast could be particularly useful for characterization of glandular malignancies (e.g., prostate, breast, and pancreas) that obstruct secretory duct lumen (reduce free water fraction)[31,32] and increase macromolecular crowding (reduce uncoordinated water fraction).[9,16] Measured as counterpart of free water diffusion, IDF suggested organ-independent b-range between 1 and 2 ms/μm^2 for effective tumor "grading." These acquisition conditions are compatible with the current clinical SOC DWI protocols allowing for retrospective analysis. This work lays ground for development of diagnostic cancer-grade assay based on quantitative IDF with potential to improve accuracy of high-grade tumor stratification from clinical DWI scans. The proposed assay may also aid radiation-free imaging protocols for active surveillance and treatment response monitoring.

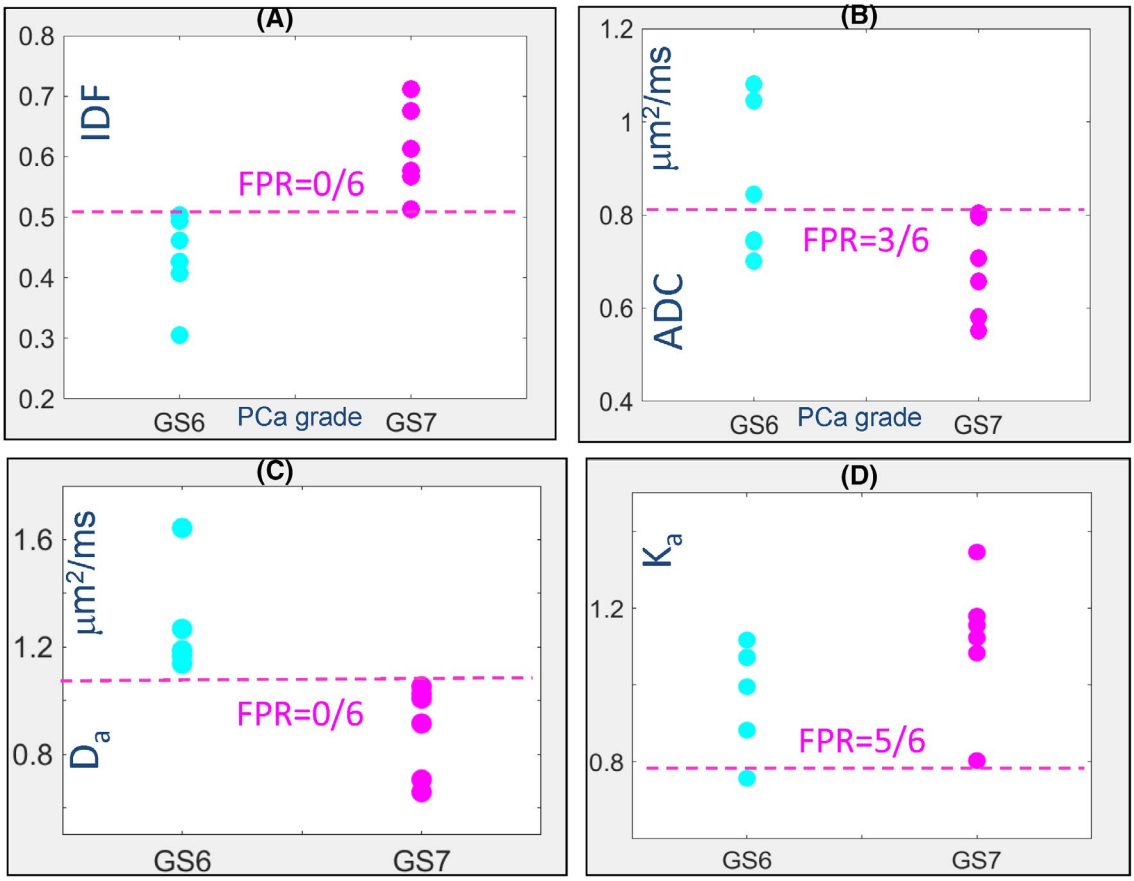

FIGURE 4 Categorical plots of ROI-mean IDF (A), PIRADS ADC (B) and apparent kurtosis diffusion parameters, D_a (C) and K_a (D), versus Gleason score (GS) for 12 PCa lesions exhibit improved false positive rate (FPR) for IDF > 0.51 and D_a < 1.05 μm²/ms compared to ADC < 0.81 μm²/ms (thresholds marked by dashed horizontal lines at highest specificity for aggressive GS7 detection)

ACKNOWLEDGMENTS

Funding support from National Institutes of Health Grants: U01CA166104, U24CA237683, R01CA249882, R01CA218144, and R01CA190299. We are thankful to University of Michigan PCa radiology experts, Dr. Davenport and Dr. Shankar who inspired this research, and Dr. Dave (Memorial Sloan Kettering) and Dr. Margolis (Cornell) for PIRADS discussions.

CONFLICT OF INTEREST

M.D., T.C., and S.S. are co-authors of IP that underlays described IDF technique assigned to and managed by the University of Michigan.

ORCID

Dariya I. Malyarenko https://orcid.org/0000-0003-0403-1501

REFERENCES

1. Le Bihan D. Apparent diffusion coefficient and beyond: what diffusion MR imaging can tell us about tissue structure. *Radiology*. 2013;268:318-322.
2. Messina C, Bignone R, Bruno A, et al. Diffusion-weighted imaging in oncology: an update. *Cancers (Basel)*. 2020;12:1493.
3. Taouli B, Beer AJ, Chenevert T, et al. Diffusion-weighted imaging outside the brain: Consensus statement from an ISMRM-sponsored workshop. *J Magn Reson Imaging*. 2016;44:521-540.
4. Iima M, Le Bihan D. Clinical intravoxel incoherent motion and diffusion MR imaging: past, present, and future. *Radiology*. 2016;278:13-32.
5. Jensen JH, Helpern JA. MRI quantification of non-Gaussian water diffusion by kurtosis analysis. *NMR Biomed*. 2010;23:698-710.
6. Panagiotaki E, Chan RW, Dikaios N, et al. Microstructural characterization of normal and malignant human prostate tissue with vascular, extracellular, and restricted diffusion for cytometry in tumours magnetic resonance imaging. *Invest Radiol*. 2015;50:218-227.
7. Cerny M, Chernyak V, Olivie D, et al. LI-RADS version 2018 ancillary features at MRI. *Radiographics*. 2018;38:1973-2001.
8. Purysko AS, Rosenkrantz AB, Barentsz JO, Weinreb JC, Macura KJ. PI-RADS version 2: a pictorial update. *Radiographics*. 2016;36:1354-1372.
9. Barkovich EJ, Shankar PR, Westphalen AC. A systematic review of the existing prostate imaging reporting and data system version 2 (PI-RADSv2) literature and subset meta-analysis of

PI-RADSv2 categories stratified by Gleason scores. *AJR Am J Roentgenol*. 2019;212:847-854.
10. Rahbar H, Zhang Z, Chenevert TL, et al. Utility of diffusion-weighted imaging to decrease unnecessary biopsies prompted by breast MRI: a trial of the ECOG-ACRIN cancer research group (A6702). *Clin Cancer Res*. 2019;25:1756-1765.
11. Shukla-Dave A, Obuchowski NA, Chenevert TL, et al. Quantitative imaging biomarkers alliance (QIBA) recommendations for improved precision of DWI and DCE-MRI derived biomarkers in multicenter oncology trials. *J Magn Reson Imaging*. 2019;49:e101-e121.
12. American Cancer Society. *Cancer Facts and Statistics 2021*. American Cancer Society, Inc; 2021 [cited 2021 August 20]. Available from: https://www.cancer.org/research/cancer-facts-statistics/all-cancer-facts-figures/cancer-facts-figures-2021.html
13. Auffenberg GB, Lane BR, Linsell S, et al. A roadmap for improving the management of favorable risk prostate cancer. *J Urology*. 2017;198:1221-1223.
14. Shankar PR, Maturen KE, George AK, et al. Temporary health impact of prostate MRI and transrectal prostate biopsy in active surveillance prostate cancer patients. *J Am Coll Radiol*. 2019;16:1385-1392.
15. European Association of Urology. *Prostate Cancer Evaluation Guidelines*. The Netherlands: European Association of Urology; Sec.6.2.1.4 2019 [cited 2021 August 20]. Available from: https://uroweb.org/guideline/prostate-cancer/
16. Hurrell SL, McGarry SD, Kaczmarowski A, et al. Optimized b-value selection for the discrimination of prostate cancer grades, including the cribriform pattern, using diffusion weighted imaging. *J Med Imaging (Bellingham)*. 2018;5:011004.
17. Hectors SJ, Semaan S, Song C, et al. Advanced diffusion-weighted imaging modeling for prostate cancer characterization: correlation with quantitative histopathologic tumor tissue composition-a hypothesis-generating study. *Radiology*. 2018;286:918-928.
18. Rosenkrantz AB, Padhani AR, Chenevert TL, et al. Body diffusion kurtosis imaging: basic principles, applications, and considerations for clinical practice. *J Magn Reson Imaging*. 2015;42:1190-1202.
19. Chatterjee A, Bourne RM, Wang SY, et al. Diagnosis of prostate cancer with noninvasive estimation of prostate tissue composition by using hybrid multidimensional MR imaging: a feasibility study. *Radiology*. 2018;287:864-873.
20. Gilani N, Malcolm P, Johnson G. A model describing diffusion in prostate cancer. *Magn Reson Med*. 2017;78:316-326.
21. Johnston EW, Bonet-Carne E, Ferizi U, et al. VERDICT MRI for prostate cancer: intracellular volume fraction versus apparent diffusion coefficient. *Radiology*. 2019;291:391-397.
22. McHugh DJ, Hubbard Cristinacce PL, Naish JH, Parker GJM. Towards a 'resolution limit' for DW-MRI tumor microstructural models: a simulation study investigating the feasibility of distinguishing between microstructural changes. *Magn Reson Med*. 2019;81:2288-2301.
23. Malyarenko DI, Swanson SD, Konar AS, et al. Multicenter repeatability study of a novel quantitative diffusion kurtosis imaging phantom. *Tomography*. 2019;5:36-43.
24. Malyarenko DI, Swanson SD, Chenevert TL, editors. Impeded diffusion fraction model for multi-exponential DWI: demonstration in kurtosis phantom and prostate cancer. In Proceedings of the ISMRM & SMRT Virtual Conference & Exhibition, 2020. Abstract PP3705.
25. Holz M, Heil SR, Sacco A. Temperature-dependent self-diffusion coefficients of water and six selected molecular liquids for calibration in accurate H-1 NMR PFG measurements. *Phys Chem Chem Phys*. 2000;2:4740-4742.
26. Polnaszek CF, Bryant RG. Self-diffusion of water at the protein surface: a measurement. *J Am Chem Soc*. 1984;106:429-430.
27. Trovato F, Tozzini V. Diffusion within the cytoplasm: a mesoscale model of interacting macromolecules. *Biophys J*. 2014;107:2579-2591.
28. Inaba T. Quantitative measurements of prostatic blood flow and blood volume by positron emission tomography. *J Urol*. 1992;148:1457-1460.
29. Rashid R, Lim NSJ, Chee SML, Png SN, Wohland T, Raghunath M. Novel use for polyvinylpyrrolidone as a macromolecular crowder for enhanced extracellular matrix deposition and cell proliferation. *Tissue Eng Part C-Me*. 2014;20:994-1002.
30. Swanson SD, Malyarenko DI, Chenevert TL, editors. Tunable diffusion kurtosis in lamellar vesicle suspensions toward development of quantitative phantom surrogate of tumor microenvironment. ISMRM 27, Montreal, Canada, 2019. Abstract TP3632.
31. Carlin D, Orton MR, Collins D, deSouza NM. Probing structure of normal and malignant prostate tissue before and after radiation therapy with luminal water fraction and diffusion-weighted MRI. *J Magn Reson Imaging*. 2019;50:619-627.
32. Devine W, Giganti F, Johnston EW, et al. Simplified luminal water imaging for the detection of prostate cancer from multiecho T-2 MR images. *J Magn Reson Imaging*. 2019;50:910-917.
33. Bojorquez JZ, Bricq S, Acquitter C, Brunotte F, Walker PM, Lalande A. What are normal relaxation times of tissues at 3 T? *Magn Reson Imaging*. 2017;35:69-80.
34. Stanisz GJ, Odrobina EE, Pun J, et al. T1, T2 relaxation and magnetization transfer in tissue at 3T. *Magn Reson Med*. 2005;54:507-512.

SUPPORTING INFORMATION

Additional supporting information may be found in the online version of the article at the publisher's website.

FIGURE S1 Summary of DWI IDF analysis workflow for physical phantom (A), and prostate cancer (PCa, b). Top left figure in (A) illustrates dynamic light scattering (DLS) measurements for V1 and V2 phantom samples with insert showing schematic of their vesicular suspension comprised of free (light blue) and impeded (dark blue) water compartments. Top right image in (A) shows phantom DWI ($b = 2$ ms/mm^2) with material vial labels and color-coded voxel locations corresponding to the IDF fit data in the lower pane legend. The chemical sample abbreviations in the legend denote CA, cetearyl alcohol; DEC, decyl alcohol; CTAB, cetyltrimethylammonium bromide; BTAC, behentriammonium chloride. Top images in (B) illustrate an example of PCa lesion annotations from whole-mount histopathology (16), registered to $b = 0$ DWI and traced on DWI ($b = 2$ ms/μm^2). Voxel samples for Gleason score

(GS) 6 and 7 and normal transition zone (nTZ), defined away from lesion boundaries are color-coded for the IDF fit data in the lower pane legend. Dashed curves in lower panes show model-based single-voxel fit for acquired log-DWI data (*) as a function of b-value (fit fractions summarized in Table S1). Arrows mark $b > 0$ subsets tested for the SOC protocols (versus all-$b > 0.1$ ms/μm^2 fit): 2 for phantom (gray and black arrows) and 1 used for PCa analysis (black arrows)

FIGURE S2 (A) Bar-plot of relative characteristics for V1/V2 and V5/V3 phantom samples is compared for DLS-derived vesicle sizes and PVP concentrations (dark green) versus different diffusion model parameters: IDF (light green), inverse ADC (dark blue), inverse apparent diffusion (cyan), and apparent kurtosis (gray, no K_a values for mono-exponential V5/V3, K_a~0). Horizontal arrows connect the diffusion parameters with the highest correlation to physical phantom properties. Magenta crosses mark the trends opposite to physical property ratios. (B) Illustrates apparent linear relation between IDF and %PVP (10% to 50%, top axis, green) and DLS vesicle size (bottom axis) for V1: DEC-CTAB, V2: CA-BTAC (cyan) and CA-CTAB (3:1 to 6:1, blue) samples. Dashed lines mark observed linear trends

Table S1 IDF model nonlinear fit fractions (±2%) for single-voxel DWI of phantom V1-V3 vials, and PCa normal transition zone (nTZ) and Gleason GS6, GS7 lesions in Figure S1

How to cite this article: Malyarenko DI, Swanson SD, McGarry SD, LaViolette PS, Chenevert TL. The impeded diffusion fraction quantitative imaging assay demonstrated in multi-exponential diffusion phantom and prostate cancer. *Magn Reson Med*. 2022;87:2053–2062. doi:10.1002/mrm.29075